Astronomy & Astrophysics manuscript no. christensen
April 22, 2014

Herschel observations of gas and dust in comet C/2006 W3 (Christensen) at 5 AU from the Sun⋆

M. de Val-Borro[1,2], D. Bockelée-Morvan[3], E. Jehin[4], P. Hartogh[1], C. Opitom[4], S. Szutowicz[5], N. Biver[3], J. Crovisier[3], D. C. Lis[6], L. Rezac[1], Th. de Graauw[7], D. Hutsemékers[4], C. Jarchow[1], M. R. Kidger[8], M. Küppers[9], L. M. Lara[10], J. Manfroid[4], M. Rengel[1], B. M. Swinyard[11,12], D. Teyssier[8], B. Vandenbussche[13], and C. Waelkens[13]

[1] Max-Planck-Institut für Sonnensystemforschung, Justus-von-Liebig-Weg 3, 37077 Göttingen, Germany
e-mail: hartogh@mps.mpg.de
[2] Department of Astrophysical Sciences, Princeton University, Princeton, NJ 08544, USA
e-mail: valborro@princeton.edu
[3] LESIA, Observatoire de Paris, CNRS, UPMC, Université Paris-Diderot, 5 place Jules Janssen, 92195 Meudon, France
[4] Institut d'Astrophysique et de Géophysique, Université de Liège, 4000 Liége, Belgium
[5] Space Research Centre, Polish Academy of Sciences, Bartycka 18A, 00-716 Warsaw, Poland
[6] California Institute of Technology, Pasadena, CA 91125, USA
[7] Joint ALMA Observatory, Alonso de Córdova 3107, Vitacura, Santiago, Chile
[8] *Herschel* Science Centre, ESAC, European Space Agency, 28691 Villanueva de la Cañada, Madrid, Spain
[9] Rosetta Science Operations Centre, ESAC, European Space Agency, 28691 Villanueva de la Cañada, Madrid, Spain
[10] Instituto de Astrofísica de Andalucía (CSIC), Glorieta de la Astronomía s/n, 18008 Granada, Spain
[11] RAL Space, Rutherford Appleton Laboratory, Chilton, Didcot OX11 0QX, UK
[12] Department of Physics and Astronomy, University College London, Gower St., London WC1E 6BT, UK
[13] Instituut voor Sterrenkunde, Katholieke Universiteit Leuven, Belgium

Received 15 January 2014 / Accepted 26 February 2014

ABSTRACT

Context. Cometary activity at large heliocentric distances is thought to be driven by outgassing of molecular species more volatile than water that are present in the nucleus. The long-period comet C/2006 W3 (Christensen) was an exceptional target for a detailed study of its distant gaseous and dust activity.

Aims. We aimed to measure the H_2O and dust production rates in C/2006 W3 (Christensen) with the *Herschel* Space Observatory at a heliocentric distance of ∼ 5 AU and compared these data with previous post-perihelion *Herschel* and ground-based observations at ∼ 3.3 AU from the Sun.

Methods. We have searched for emission in the H_2O and NH_3 ground-state rotational transitions, $J_{K_aK_c}$ (1_{10}–1_{01}) at 557 GHz and J_K (1_0–0_0) at 572 GHz, simultaneously, toward comet C/2006 W3 (Christensen) with the Heterodyne Instrument for the Far Infrared (HIFI) onboard *Herschel* on UT 1.5 September 2010. Photometric observations of the dust coma in the 70 μm and 160 μm channels were acquired with the Photodetector Array Camera and Spectrometer (PACS) instrument on UT 26.5 August 2010.

Results. A tentative 4-σ H_2O line emission feature was found in the spectra obtained with the HIFI wide-band and high-resolution spectrometers, from which we derive a water production rate of $(2.0 \pm 0.5) \times 10^{27}$ molec. s^{-1}. A 3-σ upper limit for the ammonia production rate of $< 1.5 \times 10^{27}$ molec. s^{-1} is obtained taking into account the contribution from all hyperfine components. The dust thermal emission was detected in the 70 μm and 160 μm filters, with a more extended emission in the blue channel. We fit the radial dependence of the surface brightness with radially symmetric profiles for the blue and red bands. The dust production rates, obtained for a dust size distribution index that explains the fluxes at the photocenters of the 70 μm and 160 μm PACS images, lie in the range 70 kg s^{-1} to 110 kg s^{-1}. Scaling the CO production rate measured post-perihelion at 3.20 AU and 3.32 AU, these values correspond to a dust-to-gas production rate ratio in the range 0.3–0.4.

Conclusions. The blueshift of the water line detected by HIFI suggests preferential emission from the subsolar point. However, it is also possible that water sublimation occurs in small ice-bearing grains that are emitted from an active region on the nucleus surface at a speed of ∼ 0.2 km s^{-1}. The dust production rates derived in August 2010 are roughly one order of magnitude lower than in September 2009, suggesting that the dust-to-gas production rate ratio remained approximately constant during the period when the activity became increasingly dominated by CO outgassing.

Key words. Comets: individual: C/2006 W3 (Christensen) – submillimetre: planetary systems – techniques: photometric – techniques: spectroscopic

1. Introduction

Comets are small solar system bodies with a wide range of orbital periods. They spend most of their time in the cold outer regions of the solar system, beyond the distance at which water condenses into ice grains—the so-called snow line. Therefore,

⋆ *Herschel* is an ESA space observatory with science instruments provided by European-led Principal Investigator consortia and with important participation from NASA.

they contain pristine material that reflects the chemical composition in the early solar nebula. Comets are composed of a loose aggregation of volatile icy materials and refractory particles. Observations of gas production in comets provide a unique opportunity to constrain the composition of cometary ices and to characterize a classification scheme based on their relative chemical abundances (A'Hearn et al. 1995; Biver et al. 2002b; Bockelée-Morvan et al. 2004; Crovisier et al. 2009). Studying the processes responsible for ice sublimation in comets is also important in the understanding of the activity and thermal properties of cometary nuclei. In addition, the simultaneous imaging of the thermal emission from dust particles released from the nucleus in two wavelengths bands can constrain important properties of the dust coma, such as the dust size distribution index and dust production rate (e.g., Jewitt & Luu 1990; Bockelée-Morvan et al. 2010b). Therefore, observations of cometary dust and gas can provide clues about the physical conditions in the solar nebula, and help to establish a link between the materials in the parent interstellar cloud and cometary nuclei (see e.g., Ehrenfreund et al. 2004).

Cometary activity at small heliocentric distances is driven mainly by sublimation of water molecules from the nucleus with CO_2/H_2O and CO/H_2O mixing ratios that show a great diversity and range from $\sim$ 0.01–0.1 in most cometary atmospheres (e.g., Bockelée-Morvan 2011; de Val-Borro et al. 2013). Although H_2O is generally the primary component of the nucleus, the sublimation of water is inefficient at r_h larger than 3 AU to 4 AU and the activity is dominated by molecules such as CO_2 and CO that are more volatile than water (see e.g., Bockelée-Morvan et al. 2010b; McKay et al. 2012). Therefore, the evolution of the production rate of these molecular species with heliocentric distance provides important clues for understanding the structure and composition of cometary nuclei (e.g., Biver et al. 2002a).

The *Herschel* Space Observatory (Pilbratt et al. 2010) has proven to be the most sensitive facility for directly observing water emission in distant comets and studying the chemical composition of cometary material (see e.g., Hartogh et al. 2011; Bockelée-Morvan et al. 2012; Lis et al. 2013). Water emission has been detected in the distant comet 29P/Schwassmann-Wachmann 1 (Bockelée-Morvan et al. 2010a). Moreover, recent attempts have been made to directly detect sublimating water using *Herschel* in comets C/2006 W3 (Christensen) (Bockelée-Morvan et al. 2010b) and C/2012 S1 (ISON) (O'Rourke et al. 2013a) at large heliocentric distances, and also in active objects orbiting within the main asteroid belt, that is, main-belt comets (MBCs; see e.g., de Val-Borro et al. 2012b; O'Rourke et al. 2013b).

Comet C/2006 W3 (Christensen) is a long-period comet that was discovered in November 2006 at a distance of 8.6 AU from the Sun. It passed perihelion on 6 July 2009 at a heliocentric distance of 3.13 AU. As noted previously, water ice sublimation is expected to be ineffective at large heliocentric distances and, owing to the low outgassing rate that requires very sensitive observations, it has only been directly detected previously in comet C/2006 W3 (Christensen) at infrared wavelengths in the pre-perihelion observations at 3.66 AU and 3.13 AU by the *AKARI* satellite on UT 21.1 December 2008 and UT 16.8 June 2009, respectively (Ootsubo et al. 2012).

At the time of the previous *Herschel* post-perihelion observations of comet C/2006 W3 (Christensen) at 3.3 AU from the Sun (Bockelée-Morvan et al. 2010b, hereafter Paper I) the Heterodyne Instrument for the Far Infrared (HIFI; de Graauw et al. 2010) was not available due to a single event upset in the memory of the Local Oscillator Control Unit microcontroller caused by a cosmic-particle impact. Had HIFI observations been obtained at that time, water emission in the coma would have been readily detected. Nonetheless, an upper limit to the water production rate of $< 1.4 \times 10^{28}$ molec. s^{-1} was derived from spectroscopic observations with the Photodetector Array Camera and Spectrometer (PACS; Poglitsch et al. 2010) on UT 8.8 November 2009, and an upper limit of $< 4 \times 10^{28}$ molec. s^{-1} was obtained from observations with the Spectral and Photometric Imaging REceiver (SPIRE; Griffin et al. 2010) on UT 6.6 November 2009. Additionally, the dust size distribution and dust production rate were calculated from the spectral energy distribution measured by PACS (see Paper I). Complementary production rate measurements of several species (namely CO, CH_3OH, HCN, H_2S, and OH) were obtained from the ground in pre-perihelion observations with the Nançay radio telescope and post-perihelion observations with the Institut de Radioastronomie Millimétrique (IRAM) 30-m telescope (Paper I).

Here we present the analysis of more *Herschel* outbound observations of comet C/2006 W3 (Christensen) at 5 AU from the Sun. The paper is structured as follows: in Sect. 2, we summarize the observations performed with HIFI and PACS, and the data reduction method. Section 3 presents the results of the data analysis. In Sect. 3.1, we compare the gas production rate obtained by HIFI with measurements by other facilities at various heliocentric distances. The derived dust production rates using a dust thermal emission model are compared with the values obtained in the previous PACS observations in Sect. 3.2. Finally, we discuss the main results of this work in Sect. 4 and present the conclusions in Sect. 5.

2. Observations

The *Herschel* Space Observatory is a 3.5-m telescope built and operated by the European Space Agency (ESA) covering the far-infrared and submillimetre wavelength ranges (Pilbratt et al. 2010). Comet C/2006 W3 (Christensen) (hereafter referred to as C/2006 W3) was observed with PACS and HIFI, two of the focal-plane instruments onboard *Herschel*, on UT 26.5 August and 1.5 September 2010, respectively, when the object was at $r_h \sim 5.0$ AU and a distance of Δ = 4.5–4.7 AU from the spacecraft. The observations were performed within the framework of the *Herschel* guaranteed-time key program "Water and related chemistry in the solar system" (Hartogh et al. 2009). These data complement previous outbound observations of comet C/2006 W3 obtained four months post-perihelion with PACS during the science demonstration phase on UT 1.8 and 8.8 November 2009 and with SPIRE on UT 6.6 November 2009, that have been reported previously in Paper I.

Table 1 summarizes the observing circumstances and distances to comet C/2006 W3 during the observations obtained with the HIFI and PACS instruments. We used the ephemeris provided by JPL's HORIZONS online solar system data service[1] to obtain the position and solar position angle of the comet with respect to the satellite (Giorgini et al. 1996).

The pointing information of *Herschel* observations acquired in the period between operational days (ODs) 320 and 761 suffered from a shift in the reconstructed astrometry of up to 8″ due to an introduced change in the temperature of the star-tracker. This effect was modified by a new model that was uploaded to the satellite on OD 762. For the PACS and HIFI observation of C/2006 W3 obtained on ODs 469 and 475, respectively, new

[1] http://ssd.jpl.nasa.gov/?horizons

Table 1. HIFI and PACS observing circumstances of comet C/2006 W3 (Christensen).

Date[a] (yyyy-mm-dd.ddd)	OD[b]	Inst.	ObsID	Exp. (min)	Angle[c] (°)	Scan size (′ × ′)	Speed[d] (″/s)	r_h[e] (AU)	Δ[f] (AU)	ϕ[g] (°)
2009-11-01.836	171	PACS	1 342 186 621[h]	9.4	135	9.′9 × 7.′4	10	3.33	3.56	16.°31
2009-11-01.843	171	PACS	1 342 186 622[h]	9.4	45	9.′9 × 7.′4	10	3.33	3.56	16.°31
2010-08-26.532	469	PACS	1 342 203 478	20.6	45	3.′0 × 1.′7	20	4.96	4.54	11.°22
2010-08-26.547	469	PACS	1 342 203 479	20.6	135	3.′0 × 1.′7	20	4.96	4.54	11.°22
2010-09-01.529	475	HIFI	1 342 204 014	48.0				5.00	4.68	11.°45

Notes. [(a)] UT mid-date of the observation with fractional days. [(b)] *Herschel* operational day. [(c)] Orientation angle of the scan map with respect to the detector array. [(d)] Slewing speed of the satellite along the scan line legs. [(e)] Heliocentric distance. [(f)] Distance to *Herschel*. [(g)] Solar phase angle (Sun–C/2006 W3–Earth). [(h)] Data from Paper I.

pointing products have been generated by reprocessing the data with the new astrometry generated with the *Herschel* Interactive Processing Environment (HIPE) v10.3.0 that corrects the pointing offset problem.

2.1. HIFI observations

Double-sideband (DSB) heterodyne systems such as HIFI are sensitive to two frequency ranges located on either side of the local oscillator frequency. Using HIFI, we aimed to simultaneously detect the ground-state rotational transitions $J_{K_aK_c}$ (1_{10}–1_{01}) of ortho-H_2O and J_K (1_0–0_0) of ortho-NH_3 at 557 GHz and 572 GHz, in the lower and upper sidebands (LSB and USB) of band 1b, with a total integration time of 48 min. The observation was performed in the single-point frequency-switching observing mode without a reference position on the sky that maximizes the on-target integration time, although it introduces strong standing waves in the baseline. These standing waves have to be removed and are a source of additional systematic uncertainties. A frequency throw of 94.5 MHz was applied in this observation. We simultaneously used the wide-band spectrometer (WBS) and the high-resolution spectrometer (HRS) with frequency resolutions of 1.1 MHz and 120 kHz, after resampling to a uniform frequency grid. Nonetheless, note that both the WBS and HRS spectra are oversampled and the spectrometers have a spacing of the frequency grid of ∼ 500 kHz and 60 kHz, respectively. In the HIFI observation the H_2O and NH_3 emission line frequencies were targeted in 'subband' 4 of the WBS, whereas the HRS has a single subband in the high-resolution observing mode.

The data reduction was carried out with the standard HIFI pipeline v10.3.0 using the HIPE software package to obtain calibrated level-2 products (Ott 2010). We corrected the temperature scale using the HIFI forward efficiency, i.e., the fraction of radiation received from the forward hemisphere of the beam as compared to the total radiation received by the antenna, of 0.96. Additionally a main beam efficiency of 0.75 in band 1b has been taken into account to correct for the fraction of power collected in the main Gaussian beam of the telescope with respect to the total power (see e.g., Roelfsema et al. 2012).

2.2. PACS observations

In photometer mode, the PACS instrument simultaneously images two of its three filters centered on 70 μm, 100 μm and 160 μm (referred to as red, green, and blue bands) that cover the 60–85 μm, 85–125 μm, and 125–210 μm ranges. Two bolometer arrays provide a field of view of 1.′75 × 3.′5 in each of the bands.

The PACS maps presented here were taken in the red and blue bands with two orthogonal scanning directions with respect to the detector array, using the medium slewing speed of the spacecraft along parallel lines of 20 ″/s (as compared with the slow-scan mode of 10 ″/s for the observation obtained during the *Herschel* science verification phase presented in Paper I). The integration time was 20.6 min for each scanning direction. In the earlier PACS observations from November 2009, we used three scan legs with a 9.′9 length and a ∼ 2.′5 leg separation, while the more recent observations have five scan legs with a 3′ length and 20″ separation. The pixel sizes are 6.″4×6.″4 and 3.″2×3.″2 for the red and blue channels, but for maps smaller than 5′ in size, as in the case of the C/2006 W3 observations from August 2010, the PACS photometry pipeline resamples the images to pixel sizes of 1″ and 2″ in the blue and red bands. The PACS data from November 2009 and August 2010 were reduced with the HIPE pipeline version v10.3.0.

3. Data analysis

3.1. HIFI data analysis

The data reduction for the HIFI data follows the workflow described for example in Biver et al. (2012b) and de Val-Borro et al. (2012b). After processing the raw data to calibrated level-2 products with the HIFI pipeline, the frequency-switched data are folded by averaging the original spectrum with an inverted copy that is shifted by the local oscillator throw of 94.5 MHz (e.g., Liszt 1997). A strong baseline ripple is present, introduced by multiple standing waves in the frequency-switching observing mode. To obtain a reliable estimate of the noise in the emission-free part of the spectrum, the baseline has to be removed, which was accomplished by fitting a linear combination of sine waves using the Lomb-Scargle periodogram technique (Lomb 1976; Townsend 2010). The spectrum can also be processed using an empirical mode-decomposition (EMD) method (see Rezac et al. 2014, and Rezac et al. in preparation for a quantitative comparison of Lomb-Scargle and EMD techniques with other procedures). We used a masking window of (-1,1) km s^{-1} around the transition frequency in each of the orthogonal polarizations spectra to fit the standing waves in the baseline.

The procedure used to remove the residual standing waves of frequency-switched observations introduces an additional systematic error source of about 50% of the root mean square (rms) scatter of the baseline-subtracted spectrum (see e.g., Bockelée-Morvan et al. 2012; O'Rourke et al. 2013b). Moreover, an additional uncertainty, similar to that arising from the baseline removal, is related to the flux calibration error associated with the beam efficiency error, calculated from Mars mapping observa-

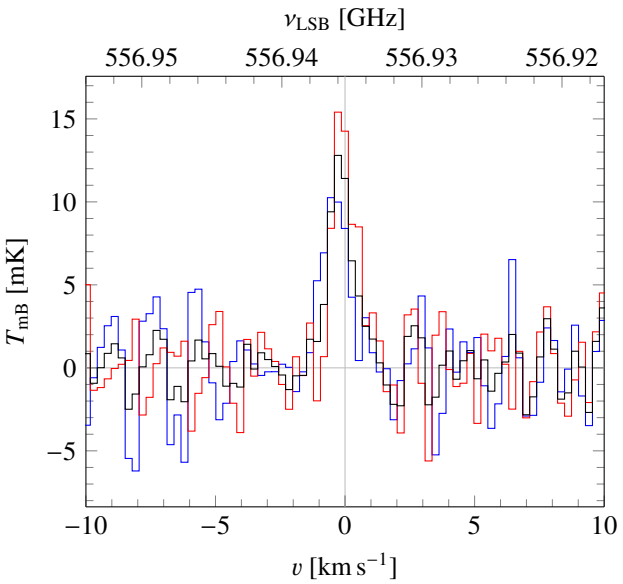

Fig. 1. Folded spectra for the horizontal polarization mixer (blue line), vertical polarization mixer (red line), and averaged spectrum (black line) of the ortho-water $J_{K_aK_c}$ (1_{10}–1_{01}) line at 556.936 GHz acquired with the WBS on UT 1.5 September 2010. The fitted baselines are obtained by masking a (-1, 1) km s^{-1} window around the rest frequency of the water line and using a linear combination of sine functions. The vertical axis is the calibrated main-beam brightness temperature, the upper horizontal axis is the lower sideband frequency, and the lower horizontal axis shows the Doppler velocity with respect to the nucleus rest frame.

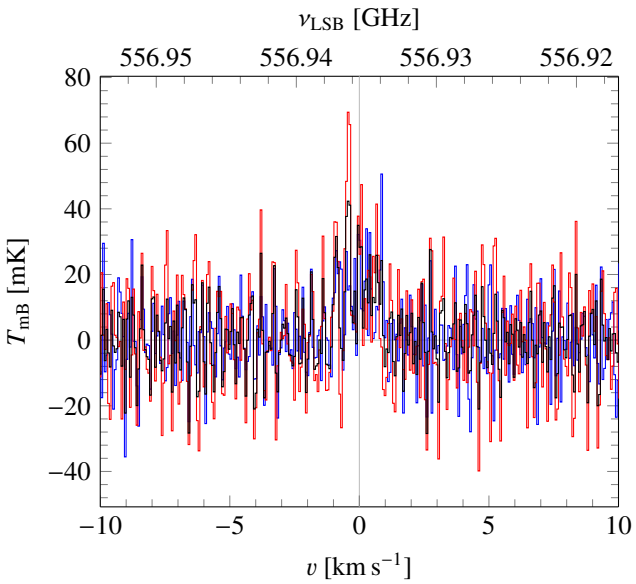

Fig. 2. Folded HRS spectra for the horizontal polarization mixer (blue line), vertical polarization mixer (red line), and averaged spectrum (black line) of the ortho-water $J_{K_aK_c}$ (1_{10}–1_{01}) line at 556.936 GHz obtained on UT 1.5 September 2010. The fitted baselines are obtained using the same method as for the WBS data. The vertical axis is the calibrated main-beam brightness temperature, the upper horizontal axis is the lower sideband frequency, and the lower horizontal axis shows the Doppler velocity with respect to the nucleus rest frame.

tions, and sideband gain ratio between the upper and lower sidebands (see Roelfsema et al. 2012). We have adopted a conservative value of 15% flux error in band 1b resulting from a combination of these uncertainties (see e.g., Higgins et al. 2014). All these systematic errors were considered in the derived line intensity and production rate uncertainties we present below.

Figure 1 shows the folded and baseline-subtracted WBS spectra of the $J_{K_aK_c}$ (1_{10}–1_{01}) transition of H_2O measured in horizontal and vertical polarizations (hereafter H and V). We averaged the H and V polarization data together to improve the signal-to-noise ratio (S/N) of the emission feature and used the same method to remove the standing waves in the baseline (black line shown in Fig. 1). A tentative detection of the H_2O line is present in the folded spectra at the position of the transition rest frequency for both polarizations. However, there are similar features in the spectrum introduced by the standing waves in the baseline ripple. The line feature is present in the folded H and V polarization spectra with a similar intensity and S/N of 3.5, although not exactly at the same frequency; the H spectrum is blueshifted by about (-240 ± 90) m s^{-1}.

Using the same method as in the WBS spectrum to fit and subtract the baseline, an emission feature appears in the HRS data that is consistent with the line area detected by the WBS within 1-σ uncertainties including the systematic component from the baseline subtraction. Figure 2 shows the reduced spectra of the water $J_{K_aK_c}$ (1_{10}–1_{01}) line measured by the HRS. Note that to use the spectrometer's native frequency resolution and to increase the S/N of the spectra, we resampled over two adjacent channels with a rectangular window function, which gives an effective spectral resolution of 120 kHz. After removing the baseline by a linear combination of sinusoids, the integrated intensities of the line are (11.4 ± 3.5) mK km s^{-1} and (16.2 ± 4.6) mK km s^{-1} in the main-beam brightness temperature scale for WBS and HRS. The agreement in the line intensities within uncertainties is to be expected since it is the same signal coming from the mixer including the standing waves, that is multiplexed to the WBS and HRS. This also confirms that the spectral feature has not been introduced by either of the two backends.

The line centroids in the HRS data with the original frequency resolution are shifted by (-230 ± 120) m s^{-1} and (-150 ± 66) m s^{-1} with respect to the rest frequency of the H_2O transition in the H and V spectra, respectively, compared to a blueshift of (-240 ± 90) m s^{-1} and (-10 ± 70) m s^{-1} for the WBS. The difference between the H and V line centroids in the HRS spectra, (-80 ± 140) m s^{-1}, is smaller than in the estimation in the WBS data, (-230 ± 120) m s^{-1}, while they agree within $\sim$ 1-σ uncertainties. Although the HRS data has higher frequency resolution than the WBS data, the S/N in the emission line in the HRS spectra is very low to allow a good estimate of the difference between the H and V line velocity offsets.

We simultaneously searched for H_2O and NH_3 emission in the HIFI observation of C/2006 W3 in the LSB and USB. The averaged spectra around the ammonia transition observed with the two HIFI backends and centered on the barycentric position of the hyperfine component frequencies are shown in Fig. 3. We removed the residual standing waves in the calibrated spectra using the same procedure as described for the H_2O emission line. There is no indication of an NH_3 line emission in either the WBS or HRS data. The derived 3-σ upper limits to the NH_3 line intensity including systematic uncertainties are < 13 mK km s^{-1} and < 17 mK km s^{-1} for the WBS and HRS spectra.

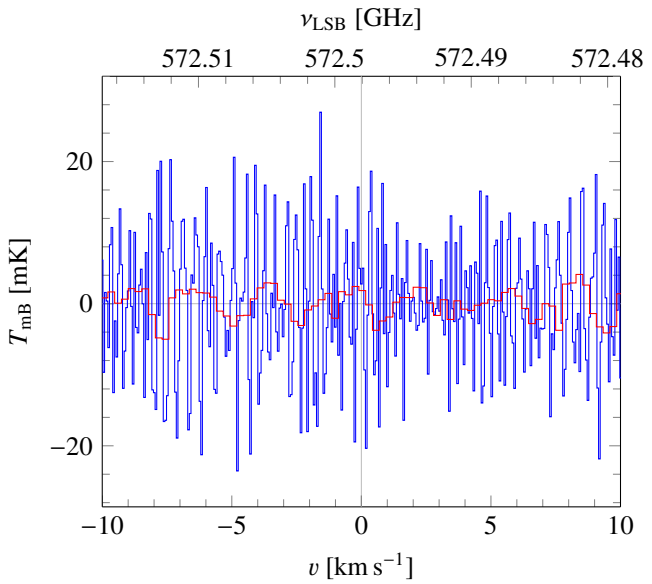

Fig. 3. Folded averaged spectra of the J_K (1_0–0_0) transition of NH_3 at 572.498 GHz obtained with the HRS (blue line) and WBS (red line) on UT 1.5 September 2010. The vertical axis is the calibrated main-beam brightness temperature, the upper horizontal axis shows the upper sideband frequency, and the lower horizontal axis shows the Doppler velocity with respect to the nucleus rest frame.

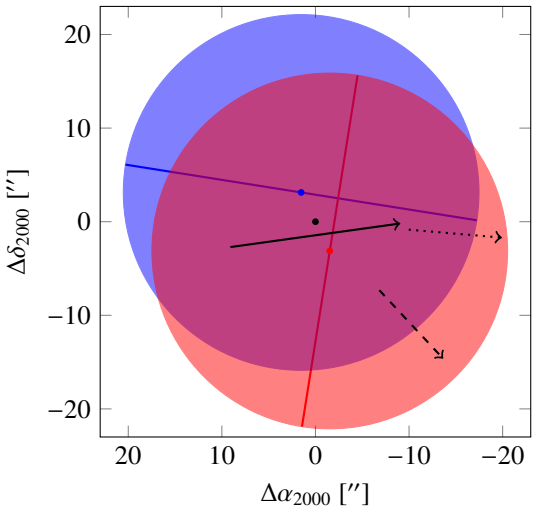

Fig. 4. Weighted average of the point spread functions (PSFs) for the horizontal polarization mixer (blue circle) and vertical polarization mixer (red circle) obtained at various times during the HIFI observation towards comet C/2006 W3 (Christensen). The orientation of the orthogonal polarizations is shown by the thick blue and red lines (H and V). The trajectory of the comet nucleus projected on the sky during the HIFI integration of 48 min is shown by the solid line according to the HORIZONS ephemeris. The projected direction toward the Sun and projected velocity vector of the comet with respect to the origin are indicated by the dotted and dashed arrows. The figure is centered on the average synthetic beam aperture located in the center of the two polarization beams and shown by the black point.

3.1.1. Origin of the difference in the H- and V-polarization spectra

The difference in the H_2O line position for the orthogonal polarizations in the HIFI WBS data can be partly explained by the pointing offset between H and V polarization spectra of ∼ 6.″6 in band 1b. A comparison of the pointing offset of the H and V beams with the full width at half maximum (FWHM) of the averaged beams is shown in Fig. 4 (∼ 38 ″ at these frequencies, corresponding to an aperture of ∼ 130 000 km at a distance of 4.68 AU from *Herschel*). For *Herschel* observations of solar system objects, the tracking mode is activated to follow their motion on the sky. In the case of comet C/2006 W3 the HORIZONS ephemeris was used to determine the tracking coefficients for the instrument boresight that are used in the pointing commands. For HIFI's band 1, the orientation of the polarization grids is such that the H polarization is basically parallel to the ecliptic plane and the V polarization lies perpendicular to it, in the case of sources close to the ecliptic plane. The projected trajectory of the comet nucleus on the sky during the observation passes farther away from the center of the averaged H beams (mean angular distance ∼ 4.″8) than from the center of the averaged V beams (mean angular distance ∼ 2.″3) as shown in Fig. 4.

As noted previously, a pointing correction due to a warm star-tracker during the HIFI observation was taken into account by the HIPE pipeline that resulted in an offset of $\cos(\delta_{\rm e}) \times (\delta_{\rm e} - \delta_{\rm o}) = 1.''0$ and $(\alpha_{\rm e} - \alpha_{\rm o}) = 2.''0$ on average over the observation, where $(\alpha_{\rm o}, \delta_{\rm o})$ and $(\alpha_{\rm e}, \delta_{\rm e})$ are the original and estimated coordinates after correction, respectively. Thus, a total offset of ∼ 2.″2 towards the northeast as compared to the original pointing, i.e., the comet position, was introduced that explains the fact that the V polarization beam is closer to the comet nucleus as shown in Fig. 4. Since we have not obtained a mapping observation with HIFI, we are not able to recover the absolute pointing offset from the morphology of the brightness distribution in the coma. However, the 1-σ pointing accuracy within the absolute pointing error (APE) is known for the epoch of the C/2006 W3 observation, and estimated to be 1.″6 after the warm star tracker correction is taken into account. The absolute pointing uncertainty introduces an additional error in the production rate estimates of about 1% that has been taken into account in their absolute standard deviations.

Owing to the small solar phase angle of ∼ 11°, the blueshift of the line in the H polarization spectrum might be caused by preferential outgassing in the direction towards the Sun within the H aperture. The smaller line shift in the V spectrum, consistent with zero offset within uncertainties, suggests a different outgassing geometry of the material comprised within the V beam. This indicates that there may be anisotropies in the coma structure in C/2006 W3 combined with possible variations in the radial and azimuthal components of the gas expansion velocity. Since the line area of the folded V spectrum is larger than the folded H spectrum and the V beam is pointing closer to the nucleus position, the difference in the line intensities in both polarizations may also arise from a higher total column density averaged within the V beam than in the H beam because of the relative pointing offset. Using the spherically symmetric ougassing model described in Sect. 3.1.2, we expect that the line intensities should decrease by ∼ 1% and 3% at 2″ and 5″ offset, respectively. These values are roughly consistent with the difference in the line intensity of the folded H and V spectra, although the deviation in the negative phase of the unfolded spectra is much larger, probably because of the poor S/N.

Considering that the integrated line of the folded and averaged WBS spectrum has an S/N of ∼ 4, it is expected that a line feature is present in both switching phases at the position of the frequency throw in the unfolded spectrum if the deteced signal is real. This aspect should also be reproducible in both polarizations with an S/N between 2–3. To test this possibility,

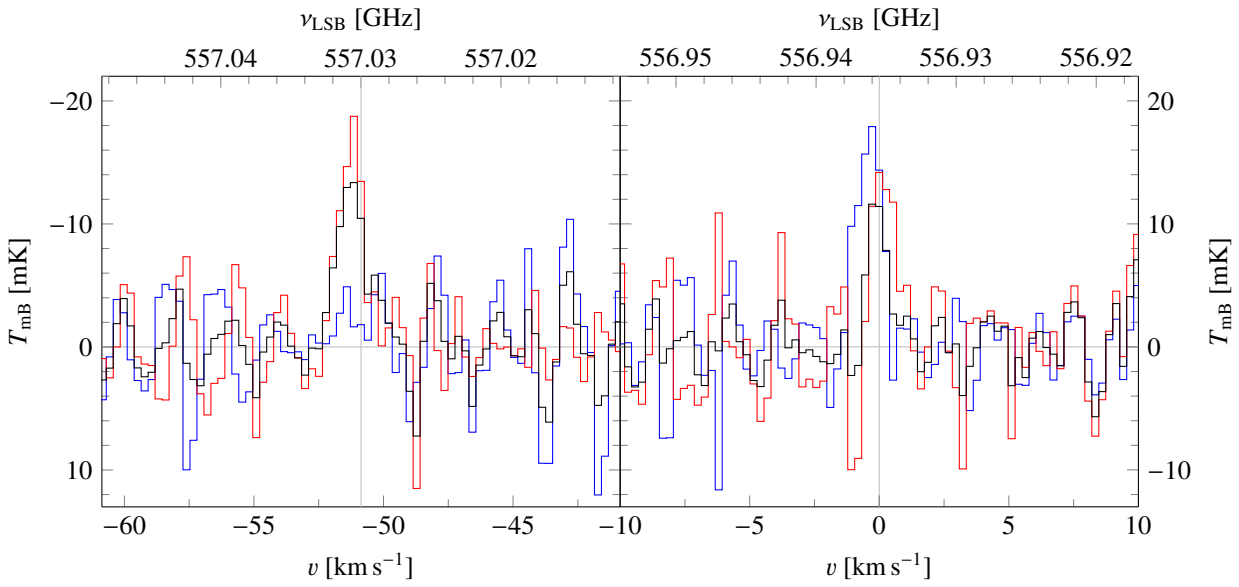

Fig. 5. Unfolded level-2 spectra for the horizontal polarization mixer (blue line), vertical polarization mixer (red line), and averaged spectrum (black line) obtained with the WBS on UT 1.5 September 2010. Baselines are fitted with a linear combination of sine functions obtained by masking (-1, 1) km s^{-1} windows around the expected position of negative (left panel) and positive (right panel) phases of the frequency-switched line rest frequency of the H_2O $J_{K_aK_c}$ (1_{10}–1_{01}) transition. Note that the scale in the vertical axes is the main brightness temperature corrected by the forward and beam efficiencies (the vertical axis scale is inverted in the left panel). The upper horizontal axis is the lower sideband frequency, and the lower horizontal axis shows the Doppler velocity with respect to the nucleus rest frame.

we searched for emission features in the unfolded WBS spectra for H and V polarizations in Fig. 5. We found evidence of an emission line feature in the positive and negative phases of the frequency-switched line frequency in the V polarization, but a feature is only present in the positive phase for the H polarization, although there is no physical reason to expect that the source has an intrisic polarization so that the line is present in only one of the polarizations. Generally, the H polarization has been found to provide better stability and a lower noise level than the V polarization (e.g., Lis et al. 2013). Since the S/N in our observation is limited, it is possible that we do not see a detection in one of the phases for the H polarization although a signal may be present.

Furthermore, it is likely that a multiple sine wave envelope does not fully account for the baseline structure around the line emission feature. In the frequency switching observing mode without a reference position, the baseline is not just a combination of sine functions. Rather, it is fundamentally the difference of the mixer response at one frequency with that at another frequency. The fine structure shape of that response will vary depending on the relative position in the intermediate frequency (IF), and this can be different in the H and V polarizations. Additionally, there is also the possibility the noise structure around the emission line in the H spectrum is particularly unfavorable, with several channels at negative noise level, creating a local drop of the same magnitude as the expected line emission signal.

3.1.2. H_2O and NH_3 production rates

To compute the production rates we used a spherically symmetric radiative transfer model that takes into account nonthermal processes and has previously been applied to analyze *Herschel* data and ground-based millimeter/submillimeter observations of line emission in cometary atmospheres (see e.g., Hartogh et al. 2010; de Val-Borro et al. 2010; Hartogh et al. 2011; de Val-Borro et al. 2012a, 2013). The excitation of water molecules was calculated with a code based on `ratran` (Hogerheijde & van der Tak 2000; Hogerheijde et al. 2009), which includes collisions between neutrals and electrons and radiation-trapping effects. We considered the effects of pumping of the vibrational excited states by infrared solar radiation. To compute the upper limit to the NH_3 production rate, the collisions with neutrals and electrons were modeled following Biver et al. (2012b).

We adopted similar parameters as in the models used to derive production rates from C/2006 W3 observations with IRAM (Paper I). Since the electron density in the coma is poorly constrained, an electron density scaling factor of $x_{n_e} = 0.2$ with respect to the standard profile derived from observations of comet 1P/Halley was used (see e.g., Biver et al. 2007; Paper I; Hartogh et al. 2010). This value was found to explain the brightness distribution of the $J_{K_aK_c}$ (1_{10}–1_{01}) water emission line obtained with mapping observations (e.g., Biver et al. 2007; Hartogh et al. 2010, 2011; Bockelée-Morvan et al. 2012). The radial number density profile for each molecule was obtained using the standard spherically symmetric Haser distribution (Haser 1957):

$$n(r) = \frac{Q}{4\pi r^2 v_{\rm exp}} \exp\left(-\frac{r\beta}{v_{\rm exp}}\right), \quad (1)$$

where Q is the total production rate of the molecule in molec. s^{-1}, $v_{\rm exp}$ is the expansion velocity in the coma, r is the nucleocentric distance, and β denotes the photodissociation rate including dissociation and ionization effects by the radiation from the Sun. The expansion velocity is assumed to be 0.4 km s^{-1} in comet C/2006 W3. This value is similar to the IRAM observations scaled to 5 AU and with the expected expansion velocity derived from the half width at half maximum (HWHM) of a Gaussian fit to the emission line of the H_2O transition observed with HIFI. For low-activity and distant comets a similar expansion velocity close to 0.5 km s^{-1} is obtained from the shapes of the OH line observed at the Nançay radio telescope (Tseng et al. 2007).

Generally, the actual outgassing geometry in cometary atmospheres can be different from the Haser density pattern used in our model. Nonetheless, the systematic errors introduced by the assumption of a spherically symmetric distribution are on the same order as the statistical errors. Provided that the model uses the same average parameters, a spherically symmetric outflow provides a similar fit to the production rate as a nonisotropic distribution consisting of a combination of several jets with variable velocity, although the shape of the derived line profile for a nonisotropic outflow may differ substantially.

Table 2 shows the line intensity and rms noise of the brightness temperature and integrated line area for each spectrometer that were used to derive the H_2O production rates and a 3-σ upper limit for the NH_3 outgassing rate. Theoretically, the HRS and WBS noise levels should be consistent taken into account the square root of the ratio of their respective resolutions, and the HRS efficiency, $\eta = 0.81$. The data have a ratio of the HRS to WBS noise that is slightly larger than the expected theoretical value.

Since CO is the most abundant species in the atmosphere of C/2006 W3 (e.g., Ootsubo et al. 2012), the main collisional excitation mechanism for H_2O molecules is collisions with CO molecules. The collisional excitation between H_2O and CO molecules was modeled using a cross section $\sigma_{CO-H_2O} \sim 0.5 \times \sigma_{H_2O-H_2O}$, where $\sigma_{H_2O-H_2O} = 5 \times 10^{-14}$ cm^2 (see Bockelée-Morvan 1987, and references therein). We also investigated a higher collision rate for H_2O of 1.5×10^{-13} cm^2, but with a Q_{CO}/Q_{H_2O} ratio of ~ 6 at 5 AU from the Sun, the retrieved Q_{H_2O} decreases by only 5%.

Using the standard deviation of the brightness temperature in the WBS backend, we derive a 3-σ upper limit for the line intensity of the NH_3 line of < 13 mK km s^{-1} over a (-1, 1) km s^{-1} window, which converts into 14.8 mK km s^{-1} taking into account losses of hyperfine structure of the line to get 100% of the line emission. For this value, an upper limit of the production rate, $Q_{NH_3} < 1.5 \times 10^{27}$ molec. s^{-1}, is derived, considering collisions with CO and using a cross section $\sigma_{CO-NH_3} = 3 \times 10^{-14}$ cm^2 (i.e. six times larger than $\sigma_{H_2O-H_2O}$). From the 3-σ upper limit for the line intensity of the HRS NH_3 spectrum of < 17 mK km s^{-1}, we derive an upper limit to the production rate of $< 1.9 \times 10^{27}$ molec. s^{-1} taking into account losses of hyperfine structure. Although the collisional cross section between CO and NH_3 is poorly determined, the dominating factor for deriving an NH_3 production rate of $< 1.5 \times 10^{27}$ molec. s^{-1} is radiative self-absorption.

There is a 60% difference in the production rate calculated in local thermodynamic equilibrium (LTE), while including only collisions between water and NH_3, the production rate Q_{NH_3} changes by 10%. Therefore, a non-LTE treatment like the escape probability method or a Monte Carlo radiative transfer approach is required to accurately compute the NH_3 population levels (Biver et al. 2012b).

Compared with the typically observed Q_{NH_3}/Q_{H_2O} mixing ratio of about 0.5–1% in comets at a heliocentric distance of 1 AU (see e.g., Biver et al. 2012b, and references therein; Biver et al. in preparation), the derived upper limit in comet C/2006 W3 of $< 1.5 \times 10^{27}$ molec. s^{-1} is on the order of the water production rate, giving a mixing ratio $Q_{NH_3}/Q_{H_2O} < 0.75$. However, because NH_3 is much more volatile than water (with a sublimation temperature, T_{sub}, of 78 K to be compared with $T_{sub} = 152$ K for H_2O) we could expect an enhanced ratio Q_{NH_3}/Q_{H_2O} closer to unity at 5 AU from the Sun. Nonetheless, a mixing ratio of $\sim 1\%$ cannot be excluded from the HIFI data.

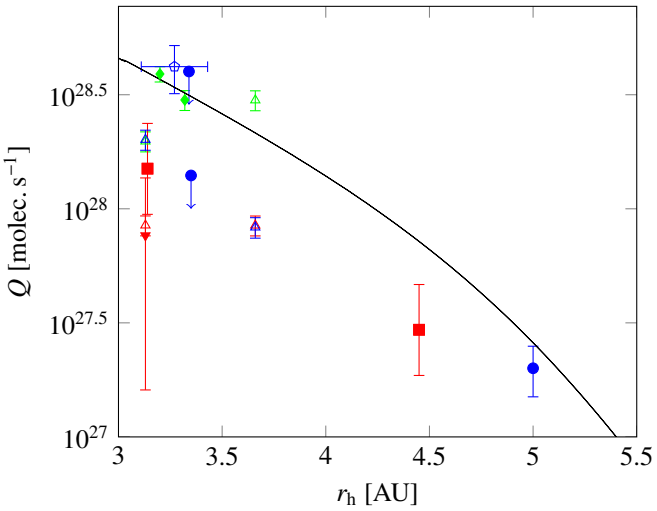

Fig. 6. H_2O (blue data points), CO_2 (red data points) and CO (green data points) production rates in comet C/2006 W3 (Christensen) as a function of heliocentric distance with 1-σ uncertainties. Open symbols show pre-perihelion production rates and filled symbols are post-perihelion rates. Circles represent detections by *Herschel* (Paper I, and this work); triangles are production rates from *AKARI* (Ootsubo et al. 2012); squares are rates measured by *Spitzer* (Reach et al. 2013); the inverted triangle is the CO_2 production rate computed from the N_{CO_2}/N_{H_2O} ratio estimated from the OI forbidden lines measured at the Apache Point Observatory 3.5-m telescope (McKay et al. 2012); diamonds are production rates obtained by the IRAM 30-m telescope, and the pentagon is the Q_{H_2O} derived from OH observations at Nançay (Paper I). The upper limits to the water production rate at about 3.3 AU were obtained by PACS and SPIRE spectroscopy (Paper I). The solid line is the water production rate by sublimation at the subsolar point on the nucleus.

3.1.3. Comparison with pre- and post-perihelion observations

The gas production rate at large heliocentric distances is controlled by sublimation of highly volatile species like carbon dioxide and carbon monoxide, which have sublimation temperatures of ~ 70 K. Although in most cometary atmospheres CO_2 has been found to dominate CO with a wide variety of mixing ratios (e.g., Ootsubo et al. 2010, 2012), the activity of C/2006 W3 was mostly driven by CO emission from the measurements obtained around 3.1–3.7 AU. Scaling the CO production rate obtained from post-perihelion measurements of the CO (2–1) line at IRAM by r_h^{-2}, as measured in comet C/1995 O1 (Hale-Bopp) (Biver et al. 1997), we estimate a mixing ratio Q_{CO}/Q_{H_2O} of 6.5 at 5 AU. These IRAM observations were obtained almost simultaneously with the PACS and SPIRE measurements from November 2009. The CO production rate measured by IRAM is about a factor of two higher than the value derived by the *AKARI* infrared observations at $r_h = 3.13$ AU (Ootsubo et al. 2012). This might be explained by the difference in the field of view of the observations and uncertainties in the coma distribution and excitation parameters (e.g., Ootsubo et al. 2012). Additionally, infrared detections of the hypervolatiles CO, CH_4 and C_2H_6 were obtained in comet C/2006 W3 using the Cryogenic Infrared Echelle Spectrograph (CRIRES) on the Very Large Telescope (VLT) at heliocentric distances of 3.25 AU and 4.03 AU, as initially reported in Bonev et al. (2010, 2013).

Figure 6 shows the H_2O, CO_2 and CO production rates as a function of heliocentric distance as measured by various instruments. The water production rate measured by HIFI and the

Table 2. Standard deviation of the brightness temperature in the HIFI spectra calculated for each spectrometer using the native spectral resolution, line intensities, line velocity shifts and retrieved H_2O and NH_3 production rates in comet C/2006 W3 (Christensen).

Molecule	Spec.	$\sigma_{T_{mB}}$ [a] (mK)	$\int T_{mB}\, dv$ (mK km s^{-1})	Δv [b] (m s^{-1})	Q [c] (molec. s^{-1})
H_2O	WBS	1.5	11.4 ± 3.5	-71 ± 40	$1.7 \pm 0.5 \times 10^{27}$
	HRS	6.3	16.2 ± 4.6	-77 ± 67	$2.3 \pm 0.7 \times 10^{27}$
NH_3	WBS	1.5	<13		<1.5 $\times 10^{27}$
	HRS	6.3	<17		<1.9 $\times 10^{27}$

Notes. [a] Standard deviation computed for frequency resolutions of 1.1 MHz and 120 kHz for WBS and HRS. [b] The velocity of the line centroids are computed using the spectra with the original frequency resolution of 500 kHz and 60 kHz for WBS and HRS. [c] Production rates or 3-σ upper limits are derived for a gas kinetic temperature of 15 K, expansion velocity of 0.4 km s^{-1}, both values being derived by scaling observations obtained at 3.3 AU from the Sun with the IRAM 30-m telescope, and an electron density scaling factor of $x_{n_e} = 0.2$ (see Paper I, and references therein).

production rate at the subsolar point on the nucleus shown by the solid curve in Fig. 6 agree but this similitude does not require water emission to come entirely from the nucleus. The solid curve represents the maximum value of water production rate because it is assumed that there is no dust on the surface and the thermal inertia of the surface ice is very low. The absorbed solar energy goes into sublimation, thermal re-radiation, and diffusion of heat into the interior of the nucleus in our model.

However, this simple model does not include release of trapped CO molecules during crystallization of amorphous water ice, gas diffusion, and re-condensation of gas in deeper, cooler layers, or sublimation of icy-dust grains in the coma. More detailed studies of the chemically differentiated nucleus and the CO sublimation are needed but they are beyond the scope of the current paper. Nonetheless, the H_2O production rate profile shown in Fig. 6 satisfies the observational data to a first approximation, as described by Szutowicz (2012). The profile was retrieved assuming a size of the active area of 48 km^2, that is, covering about 4% of the surface considering a spherical nucleus with a radius of 10 km.

It is very likely that part of the water molecules in the coma of comet C/2006 W3 at large distance from the Sun are produced by the sublimation of small icy grains (see discussion in Paper I). Evidence for sublimation from water ice grains have been observed previously by *Herschel* in other comets, for instance, C/2009 P1 (Garradd) (Bockelée-Morvan et al. 2012; Biver et al. 2012a; Bockelée-Morvan et al. 2014) and 103P/Hartley 2 (Hartogh et al. 2011; Meech et al. 2011), and at large heliocentric distance in comet C/1995 O1 (Hale–Bopp) (Davies et al. 1997). However, there is also evidence of nuclear emission in C/2006 W3; the water emission line in the averaged WBS spectrum is blueshifted by (-71 ± 40) m s^{-1}, consistent with outgassing from the nucleus in the direction towards the Sun. Nevertheless, we cannot exclude the possibility of H_2O sublimation from small ice-bearing grains outflowing from the nucleus surface in comet C/2006 W3.

3.2. PACS data analysis

We analyzed the PACS photometric observations in the same way as described in Paper I. The proper motion of the comet was relatively fast at the time of the observations, of about 10″/h, and the total integration time was ∼ 10 min to 20 min for each scanning direction in the PACS observations. Because of this, the Astronomical Observation Requests (AORs) for these observations identified comet C/2006 W3 as a moving solar system object and the nonsidereal tracking was activated by the mission planning system that lead to a continuous tracking of the motion of the comet. The HIPE pipeline that has been used to reduce the PACS observations with this special tracking mode brings all the individual frames together for each individual scan, correcting for the observed proper motion in this observing mode. For each scanning direction, individual maps were projected onto the same World Coordinate System (WCS) centered on the comet nucleus by shifting the data arrays onto a uniform grid with multivariate interpolation using a fixed Gaussian kernel. We subtracted the background emission and averaged the maps with orthogonal scanning direction, correcting for the proper motion of the target during the observations for each of the two epochs (see e.g., Santos-Sanz et al. 2012) using the ephemeris computed by the HORIZONS system (Giorgini et al. 1996). The position of the nucleus at mid-time of the observations was used to center each of the images.

Figure 7 shows the blue and red maps obtained with PACS in November 2009—presented in Paper I—and August 2010, centered on the peak position of the images after merging the observation pairs with orthogonal scan directions for each channel. The nucleus position at mid-time of the observations is shown by the yellow circles. PACS photometer observations obtained in the scan mapping mode can be affected by offsets due to the 1-σ APE of the telescope of about 1″ to 2″ at the time the C/2006 W3 observations were acquired (see Pilbratt et al. 2010; Valtchanov et al. 2013, and references therein). This value can explain the offset between the nucleus position and the estimated position of the peak shown in Fig. 7. On the other hand, the nominal relative pointing error (RPE) measured once the telescope is commanded to the target position using short observing intervals of ∼ 1 min during the performance verification (PV) phase has been found to lie in the range 0.″2–0.″3 for solar system objects within 68% confidence level. This error can generally be neglected compared with the FWHM beam sizes of 5″ and 11″ for the 70 μm and 160 μm PACS scan-mapping observations.

3.2.1. Dust coma distribution and radial profiles

The surface brightness of the 70 μm image has a broader distribution than the 160 μm image in both epochs, although the difference is significantly smaller in the August 2010 observations (see lower panel in Fig. 7). The coma distribution clearly broadens in the direction towards the Sun in the first observations, possibly due to outflow of large dust grains. In the more recent PACS maps, the red band image is elongated towards the southwest

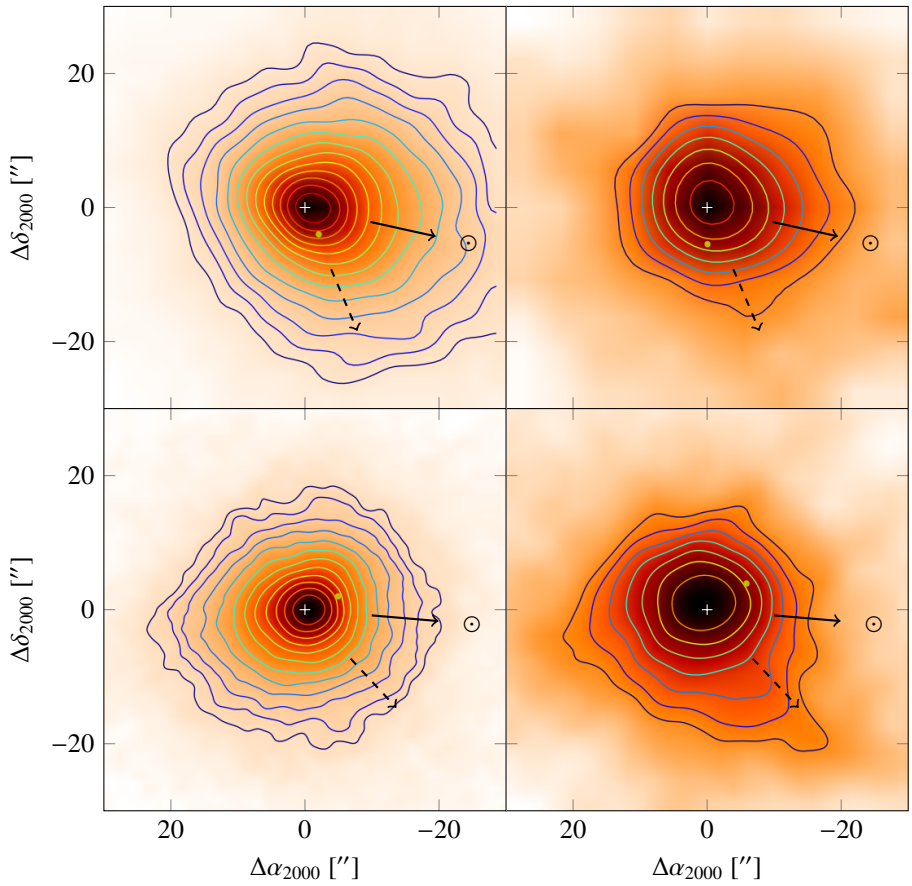

Fig. 7. Maps at 70 µm (blue band; *left column*) and 160 µm (red band; *right column*) of comet C/2006 W3 (Christensen) observed with PACS on UT 1.5 November 2009 (*upper row*, see Paper I) and UT 26.5 August 2010 (*bottom row*) centered on the peak position indicated by the white cross. The pixel sizes are 3.2″ in the blue map and 6.4″ in the red map for the November 2009 observations, and 1″ in the blue map and 2″ in the red map for the August 2010 data. Contour levels have a step of 0.1 on logarithmic scale in all the images. The position of the nucleus at the mid-time of the observations according to the HORIZONS ephemeris is shown by the yellow circle. The projected directions toward the Sun and velocity vector of the comet are indicated by the solid and dashed arrows.

close to the direction of the velocity vector of the comet, and the blue image is roughly symmetric. Note that the solar phase angle was 11° at the time of the latter observations, so the observing geometry is not the most appropriate to see an extended dust tail towards the antisolar direction. Arc-like asymmetries and spirals are observed in the 4.5 µm *Spitzer* images of C/2006 W3 when the comet was at 3.1 AU from the Sun. However, these can be explained in part by gas structures (Reach et al. 2013).

The radial profiles of surface brightness with respect to the peak position in the blue and red bands are shown in Fig. 8. We fitted the resampled radial profiles by convolving the function ρ^{-x} with a fit to the PSFs of Vesta consisting of two Gaussian functions. Figure 9 shows the radial profiles of surface brightness in the reference PSFs from Vesta data with respect to the center of the peak position in the blue and red bands, and fits to the profiles. We find that the observed surface brightness profiles of C/2006 W3 can be reproduced by exponents in the range x=0.8–0.9 in the observations from August 2010, while a value of x=1.0–1.2 better fits the profiles from November 2009 (Paper I). We do not find evidence for a substantial contribution from the nucleus thermal emission to the flux of the central pixels. A comparison with observations at optical wavelengths during the same period would provide further constraints on the dust model described in Section 3.2.2, but these observations are not available in the literature.

Table 3. Flux densities from PACS observations of comet C/2006 W3 (Christensen).

Date	Flux at photocenter[a]	
	70 µm	160 µm
(yyyy-mm-dd)	(mJy/pxl)	(mJy/pxl)
2009-11-01[b]	37.3 ± 0.2	5.0 ± 0.3
2010-08-26	8.6 ± 0.2	1.27 ± 0.06

Notes. [(a)] The pixel size is 1″ for both channels. The quoted error bar does not take into account a 5% uncertainty in the flux calibration. [(b)] Data from Paper I.

3.2.2. Dust size distribution and production rates

To determine the dust production rate $Q_{\rm dust}$, we compared the flux densities measured on the brightest pixels of the blue and red PACS maps with those expected from a model of dust thermal emission. Table 3 shows the measured flux densities at photocenter by PACS above the background noise in the two observing epochs.

The model used for this study is the same as that applied to the PACS data of comet C/2006 W3 obtained in 2009 at 3.35 AU from the Sun (Paper I), comet C/2012 S1 (ISON) (O'Rourke et al. 2013a) and of the centaurs 2060 Chiron and

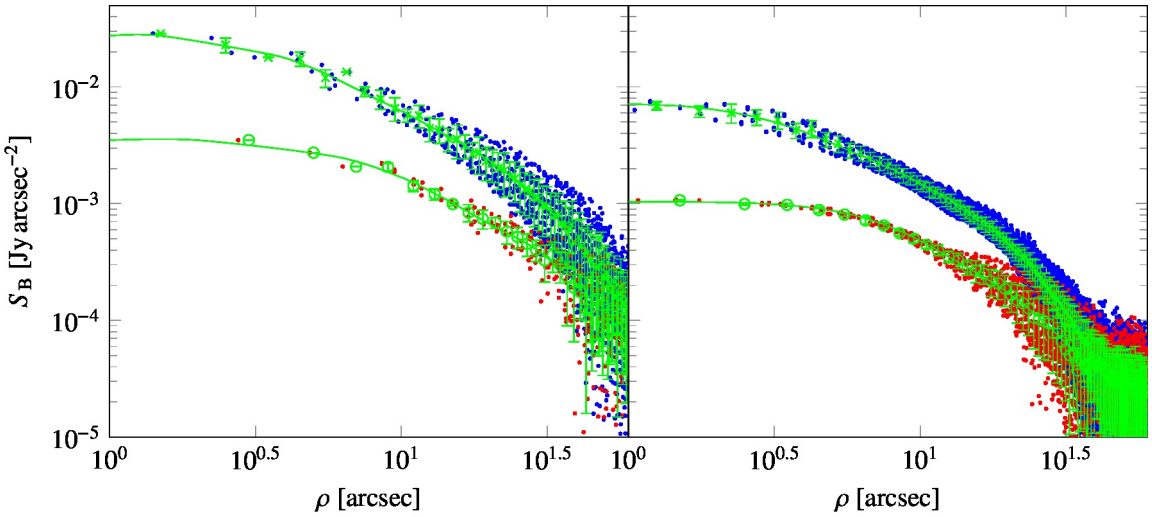

Fig. 8. *Left panel*: surface brightness in comet C/2006 W3 (Christensen) as a function of distance from the position of the center of the peak measured with PACS on UT 1.8 November 2009 (shown by the blue and red dots for the 70 μm and 160 μm bands with a pixel size of 3.″2 and 6.″4). *Right panel*: surface brightness radial profiles observed on UT 26.5 August 2010 (blue and red dots denote the 70 μm and 160 μm bands with projected pixel size of 1″ and 2″). The green crosses and circles are resampled profiles with 1″ and 2″ bins for the blue and red band images from November 2009, and 0.″5 and 1″ bins for the blue and red band images from August 2010. Error bars are 1-σ statistical uncertainties.

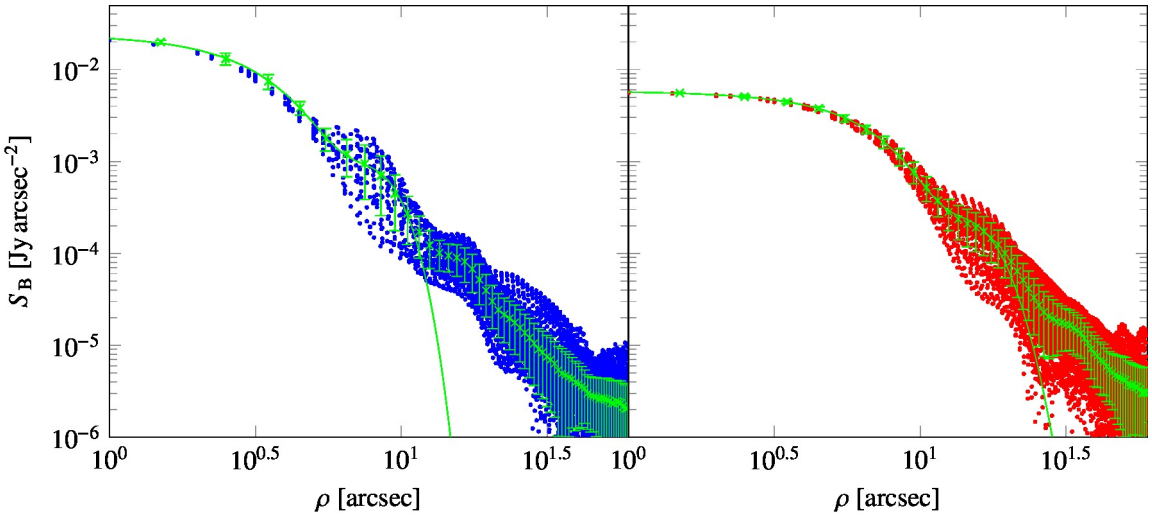

Fig. 9. Radial PSF profiles from PACS observations of the main-belt asteroid Vesta in the blue (70 μm; *left panel*) and red (160 μm; *right panel*) channels. The green crosses are the resampled data using a 1″ bin with 1-σ statistical uncertainties. Solid lines are fits to the resampled PSF profiles using a sum of two Gaussian functions.

10199 Chariklo (Fornasier et al. 2013). The basic principles of this model are given in Jewitt & Luu (1990). Absorption cross-sections calculated with the Mie theory were used to compute the temperature of the grains, solving the equation of radiative equilibrium, and their thermal emission. Complex refractive indices of amorphous carbon and olivine (Mg:Fe = 50:50) (Edoh 1983; Dorschner et al. 1995) were taken as broadly representative of cometary dust.

We considered a differential dust production $Q_{\rm dust}(a)$ as a function of grain radius a, described by the size index α. The size-dependent grain velocities $v_{\rm dust}(a)$, as well as the maximum grain radius $a_{\rm max}$, were computed following Crifo & Rodionov (1997). We assumed a nucleus bulk density of 500 kgm^{-3}, consistent with observational constraints (Davidsson et al. 2007; Richardson et al. 2007; Thomas et al. 2013) and the same value for the dust density consistent with the average density of the "fluffy" dust particles found in the coma of comet 81P/Wild 2 (Niimi et al. 2012).

The maximum grain size and dust velocities critically depend on the nucleus size and the gas production rate at the surface, which are both poorly constrained in C/2006 W3. For the nominal value of the nucleus size, our model assumes a nucleus radius of $R_{\rm N}$ = 10 km, as in Paper I.

Measurements of the CO and CO_2 production rates in the heliocentric range $r_{\rm h}$ = 3.1–3.7 AU (Fig. 4) show that the distant activity of comet C/2006 W3 was CO-dominated, with a $Q_{\rm CO_2}/Q_{\rm CO}$ production rate ratio of typically 0.3–0.4 (Ootsubo et al. 2012; McKay et al. 2012). From the intensity of the emission observed in the wide 4.5-μm *Spitzer* filters on 9 July 2010 at 4.45 AU post-perihelion (Reach et al. 2013), which mixes the contributions of fluorescence emission from CO_2 and CO, we estimate the CO production rate to be $\sim 8 \times 10^{27}$ molec. s^{-1} at that time. On the other hand, the extrapolation of the helio-

Table 4. Dust model parameters and dust production rates of comet C/2006 W3 (Christensen) derived from PACS 70 μm and 160 μm data for carbon and olivine grains.

Date	r_h	Q_{CO}	a_{max}	v_{dust} [a]		α	Q_{carbon} [b]		$Q_{olivine}$ [b]	
				a_{min}	a_{max}		70 μm	160 μm	70 μm	160 μm
(yyyy-mm-dd)	(AU)	(molec. s^{-1})	(mm)	(m s^{-1})	(m s^{-1})		(kg s^{-1})	(kg s^{-1})	(kg s^{-1})	(kg s^{-1})
2009-11-08	3.35	3×10^{28}	0.59[c]	5.7	174	−3	1520	1092	923	1190
						−3.5	923	884	676	965
						−4	650	900	606	1220
2010-08-26	4.96	4×10^{27}	0.07	6.3	106[d]	−3	89	56	63	76
						−3.5	82	68	70	102
						−4	98	112	96	182
2010-08-26	4.96	8×10^{27}	0.14	6.3	131[d]	−3	172	102	113	109
						−3.5	139	104	109	130
						−4	140	153	133	221

Notes. [(a)] Dust velocities for sizes a_{min} and a_{max}, with $a_{min} = 0.1$ μm. [(b)] Dust production rate derived assuming $a_{min} = 0.1$ μm. [(c)] In Paper I, the maximum size computed by our dust model was multiplied by 1.5 to better match state-of-the-art hydrodynamic simulations (see Crifo et al. 2005, and references therein). [(d)] The velocity of 1-μm sized particles is 45 m s^{-1} and 60 m s^{-1} for $Q_{CO} = 4 \times 10^{27}$ molec. s^{-1} and 8×10^{27} molec. s^{-1}, respectively.

centric variation of Q_{CO} from 3.66 AU to 4.45 AU measured by *AKARI* and *Spitzer* (Ootsubo et al. 2012; Reach et al. 2013), to the heliocentric distance ($r_h = 4.96$ AU), corresponding to the date of the PACS measurements from 26 August 2010, yields $Q_{CO} = 4 \times 10^{27}$ molec. s^{-1}. Therefore, we considered a CO production rate of 4×10^{27} molec. s^{-1} and 8×10^{27} molec. s^{-1} in our modeling, referred to as low- and high-activity cases.

Table 4 presents the maximum dust size and the range of dust velocities computed by our dust model. Results for 8 November 2009 (Paper I) and 26 August 2010 are presented in the table. In September 2009 at $r_h = 3.35$ AU, the CO production rate was measured to be $Q_{CO} = 3 \times 10^{28}$ molec. s^{-1} with the IRAM 30-m telescope (Paper I), and this value was used to calculate the dust parameters (Table 4). We considered two different CO production rates for the August 2010 observations.

Dust production rates derived from the 70-μm and 160-μm maps of 26 August 2010 agree within a factor of 1.7 or lower, depending on the size index (Table 4). For the high-activity case and olivine grains, the best agreement is found for a size index $\alpha \sim -3.3$, while for carbon grains the best fit is for $\alpha \sim -4$. For the low-activity case, the best fit is for $\alpha > -3$ and $\alpha \sim -4$ for carbon and olivine grains. In conclusion, the PACS data of August 2010 suggest a size index between −4 and −3, consistent with the value $\alpha = -3.6^{+0.25}_{-0.8}$ derived in Paper I from the August 2009 data. For the size indexes that explain the fluxes at the photocenters of the 70 μm and 160 μm maps, we infer dust production rates in the range 70 kg s^{-1} to 110 kg s^{-1} at 4.96 AU from the Sun (Table 4). This corresponds to a dust-to-gas production rate ratio of 0.3–0.4. The dust production rate derived in August 2010 is one order of magnitude lower than in November 2009, similar to the CO production rate difference in the same period (Table 4, Paper I), suggesting that the dust-to-gas production rate ratio remained approximately constant from 3.35 AU to 4.96 AU. When considering a nucleus radius of $R_N = 5$ km instead of 10 km, the inferred dust production rates and dust-to-gas ratios are typically twice as high, while the dust-to-gas production rate ratio remains constant over those heliocentric distances.

4. Discussion

We studied the gas and dust activity in the long-period comet C/2006 W3 (Christensen) using remote-sensing observations obtained with the *Herschel* Space Observatory at 5.0 AU from the Sun. A tentative detection of the ortho-H_2O ground-state transition is observed in the HIFI spectra with 4-σ significance. Even though the H_2O line is only marginally detected, the derived H_2O production rate and line shape and velocity shift are consistent with the emission feature having a cometary origin. We derive a water production rate of $(2.0 \pm 0.5) \times 10^{27}$ molec. s^{-1} using a spherically symmetric radiative transfer model. Concurrently, we aimed to detect the ground-state rotational transitions of ortho-NH_3 in the USB of HIFI's band 1b, from which a 3-σ upper limit for the ammonia production rate of $< 1.5 \times 10^{27}$ molec. s^{-1} is derived, corresponding to a mixing ratio $Q_{NH_3}/Q_{H_2O} < 0.75$.

Water sublimates fully at heliocentric distances < 2.5 AU and is responsible for the activity of cometary nuclei at these distances form the Sun, while its sublimation becomes inefficient at larger distances where the nucleus surface temperature may be lower than the H_2O sublimation temperature (Crovisier & Encrenaz 2000). Thus, outgassing activity at heliocentric distances > 3 AU is mostly driven by molecular species more volatile than water such as carbon monoxide. To date, the largest heliocentric distance at which OH emission—which is regarded as a proxy for H_2O—has been detected is 4.7 AU, in preperihelion observations of the exceptionally active comet C/1995 O1 (Hale–Bopp) with the Nançay radio telescope (Colom et al. 1999).

Whether the observed water emission in C/2006 W3 originates directly in the nucleus or it is produced by icy grains in the coma can be partly assessed from the shape of the emission line. The characteristic blueshift of the water line detected by the H polarization WBS spectrum is indicative of preferential emission from the daytime hemisphere in the direction towards the Sun, taking into account the small solar phase angle of ∼ 11° at the time of the observations. The smaller blueshift of the line in the V polarization WBS spectrum suggests that the material in the coma has a nonspherical outgassing geometry with possibly variable gas velocity. However, from the HIFI observations we

cannot exclude the possibility that water sublimation occurs in small icy grains outflowing at a speed close to 0.2 km s^{-1} from the nucleus surface.

Production rates of several species measured with ground-based and space observatories at different heliocentric distances were compared with the H_2O production rate derived from the *Herschel* observations. The gas production rate in C/2006 W3 is driven by sublimation of hyper-volatile carbon monoxide molecules, while CO_2 has been found to dominate CO with a wide variety of mixing ratios in most comets (e.g., Ootsubo et al. 2010; A'Hearn et al. 2011; Ootsubo et al. 2012). Since CO is more volatile than CO_2, CO may be depleted in the surface layers of comets after multiple passages through the inner solar system, and the CO enrichment measured in C/2006 W3 may indicate that of the primordial material of the early solar nebula (Ootsubo et al. 2012). We find that the evolution of the water production rate is consistent with an estimate of the water vapor outgassing from the subsolar point. However, more sophisticated thermal models considering the chemical differentiation of the nucleus and emission from icy grains that were ejected from a localized region may lead to slightly different profiles and smaller active area (Kossacki and Szutowicz in preparation).

The thermal emission from the dust in the coma is detected by PACS photometric observations in the blue and red channels. The asymmetry in the red image indicates an anisotropic emission from the subsolar point on the nucleus, consistent with the H_2O line blueshift. Dust production rates were computed for low (4×10^{27} molec. s^{-1}) and high (8×10^{27} molec. s^{-1}) CO production rates and for the case of amorphous carbon and olivine grains using the dust model described in Paper I. By comparing the flux density at the optocenter in the blue and red bands with the dust thermal emission in the model, we derived the dust production rates. For a dust size distribution index that explains the fluxes at the photocenters of the 70 μm and 160 μm PACS images, the dust production rate is in the range of 70 kg s^{-1} to 110 kg s^{-1} at the time of the PACS observations in August 2010, for the low and high outgassing cases. These values of the production rate correspond to a dust-to-gas production rate ratio of 0.3–0.4.

The dust production rates derived in the August 2010 observations are roughly one order of magnitude lower than those in September 2009 from the PACS observations (see Table 4 and Paper I), while the CO production rate similarly varies in the same time span assuming a post-perihelion trend $\propto r_h^{-2}$, as measured in comet C/1995 O1 (Hale-Bopp) (Biver et al. 1997). This indicates that the dust-to-gas production rate ratio remained approximately constant during the time when the gas activity of the comet became increasingly dominated by CO outgassing. We find that the PACS data of August 2010 is best fitted by a size index between −4 and −3, consistent with the value derived from the August 2009 PACS data (Paper I).

5. Conclusions

Combining observations of rotational emission lines and dust thermal emission provide valuable constraints on the properties of the gaseous and dust activity in comets. The *Herschel* Space Observatory was a unique facility for obtaining sensitive observations of water emission in comets at large heliocentric distances (e.g., Bockelée-Morvan et al. 2010a; O'Rourke et al. 2013a), and imaging the thermal dust coma in two channels simultaneously at far infrared wavelengths (see e.g., Paper I; Meech et al. 2011).

We presented HIFI and PACS observations of comet C/2006 W3 that will be an additional constraint in understanding the physical processes responsible for the distant activity in comets. These observations will complement previous measurements of C/2006 W3 obtained with other facilities at smaller heliocentric distances (see e.g., Paper I; Ootsubo et al. 2012; McKay et al. 2012; Reach et al. 2013; Bonev et al. 2013) that confirm that the activity of this object is dominated by sublimation of molecular species more volatile than H_2O. These data will also add another set of data points to the available observations of the distant activity of other comets such as 29P/Schwassmann-Wachmann 1 (Bockelée-Morvan et al. 2010a) and C/1995 O1 (Hale-Bopp) (e.g. Biver et al. 2002a; Rauer et al. 2003).

Acknowledgements. HIFI has been designed and built by a consortium of institutes and university departments from across Europe, Canada, and the United States under the leadership of SRON, Netherlands Institute for Space Research, Groningen, The Netherlands, and with major contributions from Germany, France, and the US. Consortium members are: Canada: CSA, U.Waterloo; France: CESR, LAB, LERMA, IRAM; Germany: KOSMA, MPIfR, MPS; Ireland, NUI Maynooth; Italy: ASI, IFSI-INAF, Osservatorio Astrofisico di Arcetri-INAF; Netherlands: SRON, TUD; Poland: CAMK, CBK; Spain: Observatorio Astronómico Nacional (IGN), Centro de Astrobiología (CSIC-INTA). Sweden: Chalmers University of Technology – MC2, RSS & GARD; Onsala Space Observatory; Swedish National Space Board, Stockholm University – Stockholm Observatory; Switzerland: ETH Zurich, FHNW; USA: Caltech, JPL, NHSC. PACS has been developed by a consortium of institutes led by MPE (Germany) and including UVIE (Austria); KU Leuven, CSL, IMEC (Belgium); CEA, LAM (France); MPIA (Germany); INAF-IFSI/OAA/OAP/OAT, LENS, SISSA (Italy); IAC (Spain). This development has been supported by the funding agencies BMVIT (Austria), ESA-PRODEX (Belgium), CEA/CNES (France), DLR (Germany), ASI/INAF (Italy), and CICYT/MCYT (Spain). Support for this work was provided by NASA through an award issued by JPL/Caltech. We thank M. Sánchez-Portal from the *Herschel* Science Center, and H. Linz from the PACS Instrument Control Center (ICC) for their help with the reduction and analysis of the *Herschel* data. The anonymous referee is thanked for providing constructive comments and help in improving the contents of the paper. M.dV.B. acknowledges partial support from grants NSF AST-1108686 and NASA NNX12AH91H. E.J. is FNRS Research Associate, D.H. is Senior Research Associate and J.M. is Research Director FNRS. C.O. thanks the Belgian FNRS for funding her PhD thesis. S.S. acknowledges support from Polish MNiSW under grant 181/N-HSO/2008/0. L.R. was supported by the Special Priority Program 1488 (PlanetMag, `http://www.planetmag.de`) of the German Science Foundation.

References

A'Hearn, M. F., Belton, M. J. S., Delamere, W. A., et al. 2011, Science, 332, 1396
A'Hearn, M. F., Millis, R. L., Schleicher, D. G., Osip, D. J., & Birch, P. V. 1995, Icarus, 118, 223
Biver, N., Bockelée-Morvan, D., Colom, P., et al. 1997, Earth Moon and Planets, 78, 5
Biver, N., Bockelée-Morvan, D., Colom, P., et al. 2002a, Earth Moon and Planets, 90, 5
Biver, N., Bockelée-Morvan, D., Crovisier, J., et al. 2002b, Earth Moon and Planets, 90, 323
Biver, N., Bockelée-Morvan, D., Crovisier, J., et al. 2007, Planet. Space Sci., 55, 1058
Biver, N., Bockelée-Morvan, D., Lis, D. C., et al. 2012a, LPI Contributions, 1667, 6330
Biver, N., Crovisier, J., Bockelée-Morvan, D., et al. 2012b, A&A, 539, A68
Bockelée-Morvan, D. 1987, A&A, 181, 169
Bockelée-Morvan, D. 2011, in IAU Symposium No. 280, 261–274
Bockelée-Morvan, D., Biver, N., Crovisier, J., et al. 2010a, in BAAS, Vol. 42, 946
Bockelée-Morvan, D., Biver, N., Crovisier, J., et al. 2014, A&A, 562, A5
Bockelée-Morvan, D., Biver, N., Swinyard, B., et al. 2012, A&A, 544, L15
Bockelée-Morvan, D., Crovisier, J., Mumma, M. J., & Weaver, H. A. 2004, in Comets II, ed. M. C. Festou, H. U. Keller, & H. A. Weaver (Univ. Arizona Press), 391–423
Bockelée-Morvan, D., Hartogh, P., Crovisier, J., et al. 2010b, A&A, 518, L149
Bonev, B., Böhnhardt, H., Mumma, M. J., et al. 2010, in BAAS, Vol. 42, 963

Bonev, B. P., Mumma, M. J., Villanueva, G. L., et al. 2013, in BAAS, Vol. 45, 413.18
Colom, P., Gérard, E., Crovisier, J., et al. 1999, Earth Moon and Planets, 78, 37
Crifo, J.-F., Loukianov, G. A., Rodionov, A. V., & Zakharov, V. V. 2005, Icarus, 176, 192
Crifo, J. F. & Rodionov, A. V. 1997, Icarus, 127, 319
Crovisier, J., Biver, N., Bockelée-Morvan, D., et al. 2009, Earth Moon and Planets, 105, 267
Crovisier, J. & Encrenaz, T., eds. 2000, Comet science : the study of remnants from the birth of the solar system (Cambridge University Press)
Davidsson, B. J. R., Gutiérrez, P. J., & Rickman, H. 2007, Icarus, 187, 306
Davies, J. K., Roush, T. L., Cruikshank, D. P., et al. 1997, Icarus, 127, 238
de Graauw, T., Helmich, F. P., Phillips, T. G., et al. 2010, A&A, 518, L6
de Val-Borro, M., Hartogh, P., Crovisier, J., et al. 2010, A&A, 521, L50
de Val-Borro, M., Hartogh, P., Jarchow, C., et al. 2012a, A&A, 545, A2
de Val-Borro, M., Küppers, M., Hartogh, P., et al. 2013, A&A, 559, A48
de Val-Borro, M., Rezac, L., Hartogh, P., et al. 2012b, A&A, 546, L4
Dorschner, J., Begemann, B., Henning, T., Jaeger, C., & Mutschke, H. 1995, A&A, 300, 503
Edoh, J. H. 1983, Ph.D. thesis, Univ. Arizona
Ehrenfreund, P., Charnley, S. B., & Wooden, D. 2004, in Comets II, ed. M. C. Festou, H. U. Keller, & H. A. Weaver (Univ. Arizona Press), 115–133
Fornasier, S., Lellouch, E., Müller, T., et al. 2013, A&A, 555, A15
Giorgini, J. D., Yeomans, D. K., Chamberlin, A. B., et al. 1996, in BAAS, Vol. 28, 1158
Griffin, M. J., Abergel, A., Abreu, A., et al. 2010, A&A, 518, L3
Hartogh, P., Crovisier, J., de Val-Borro, M., et al. 2010, A&A, 518, L150
Hartogh, P., Lellouch, E., Crovisier, J., et al. 2009, Planet. Space Sci., 57, 1596
Hartogh, P., Lis, D. C., Bockelée-Morvan, D., et al. 2011, Nature, 478, 218
Haser, L. 1957, Bull. Soc. Roy. Sci. Liège, 43, 740
Higgins, R., Teyssier, D., Braine, J., et al. 2014, Exp. Astron., in press
Hogerheijde, M. R., Qi, C., de Pater, I., et al. 2009, AJ, 137, 4837
Hogerheijde, M. R. & van der Tak, F. F. S. 2000, A&A, 362, 697
Jewitt, D. & Luu, J. 1990, ApJ, 365, 738
Lis, D. C., Biver, N., Bockelée-Morvan, D., et al. 2013, ApJ, 774, L3
Liszt, H. 1997, A&AS, 124, 183
Lomb, N. R. 1976, Ap&SS, 39, 447
McKay, A. J., Chanover, N. J., Morgenthaler, J. P., et al. 2012, Icarus, 220, 277
Meech, K. J., A'Hearn, M. F., Adams, J. A., et al. 2011, ApJ, 734, L1
Niimi, R., Kadono, T., Tsuchiyama, A., et al. 2012, ApJ, 744, 18
Ootsubo, T., Kawakita, H., Hamada, S., et al. 2012, ApJ, 752, 15
Ootsubo, T., Usui, F., Kawakita, H., et al. 2010, ApJ, 717, L66
O'Rourke, L., Bockelée-Morvan, D., Biver, N., et al. 2013a, A&A, 560, A101
O'Rourke, L., Snodgrass, C., de Val-Borro, M., et al. 2013b, ApJ, 774, L13
Ott, S. 2010, in Astronomical Data Analysis Software and Systems XIX, Vol. 434, ASP Conf. Ser., ed. Y. Mizumoto, K.-I. Morita, & M. Ohishi, 139
Pilbratt, G. L., Riedinger, J. R., Passvogel, T., et al. 2010, A&A, 518, L1
Poglitsch, A., Waelkens, C., Geis, N., et al. 2010, A&A, 518, L2
Rauer, H., Helbert, J., Arpigny, C., et al. 2003, A&A, 397, 1109
Reach, W. T., Kelley, M. S., & Vaubaillon, J. 2013, Icarus, 226, 777
Rezac, L., de Val-Borro, M., Hartogh, P., et al. 2014, A&A, 563, A4
Richardson, J. E., Melosh, H. J., Lisse, C. M., & Carcich, B. 2007, Icarus, 191, 176
Roelfsema, P. R., Helmich, F. P., Teyssier, D., et al. 2012, A&A, 537, A17
Santos-Sanz, P., Lellouch, E., Fornasier, S., et al. 2012, A&A, 541, A92
Szutowicz, S. 2012, LPI Contributions, 1667, 6192
Thomas, P. C., A'Hearn, M. F., Veverka, J., et al. 2013, Icarus, 222, 550
Townsend, R. H. D. 2010, ApJS, 191, 247
Tseng, W.-L., Bockelée-Morvan, D., Crovisier, J., Colom, P., & Ip, W.-H. 2007, A&A, 467, 729
Valtchanov, I., Hopwood, R., Polehampton, E., et al. 2013, Exp. Astron., 1